






RESEARCH ARTICLE | AUGUST 01 2022

Self-pulsing and chaos in the asymmetrically driven dissipative photonic Bose–Hubbard dimer: A bifurcation analysis

Jesús Yelo-Sarrión   ; Francois Leo  ; Simon-Pierre Gorza  ; Pedro Parra-Rivas 



Chaos 32, 083103 (2022)

<https://doi.org/10.1063/5.0088597>



View
Online



Export
Citation

CrossMark

Articles You May Be Interested In

Hybrid organic-inorganic coatings based on alkoxy-terminated macromonomers

AIP Conference Proceedings (January 1996)

Manifestation of the upper Hubbard band in the 2D Hubbard model at low electron density

Low Temperature Physics (October 2011)

The Hubbard transition and unsaturated hydrocarbons

J. Chem. Phys. (March 1989)

14 September 2023 07:25:06

AIP Advances

Why Publish With Us?



25 DAYS
average time
to 1st decision



740+ DOWNLOADS
average per article



INCLUSIVE
scope

[Learn More](#)

Self-pulsing and chaos in the asymmetrically driven dissipative photonic Bose–Hubbard dimer: A bifurcation analysis

Cite as: Chaos 32, 083103 (2022); doi: 10.1063/5.0088597

Submitted: 18 February 2022 · Accepted: 15 June 2022 ·

Published Online: 1 August 2022



View Online



Export Citation



CrossMark

Jesús Yelo-Sarrión,^{1,a)} Francoio Leo,¹ Simon-Pierre Gorza,¹ and Pedro Parra-Rivas^{1,2,b)}

AFFILIATIONS

¹OPERA-Photonique, Université libre de Bruxelles, 50 Avenue F. D. Roosevelt, CP 194/5, B-1050 Bruxelles, Belgium

²Dipartimento di Ingegneria dell'Informazione, Elettronica e Telecomunicazioni, Sapienza Università di Roma, via Eudossiana 18, 00184 Rome, Italy

^{a)}Author to whom correspondence should be addressed: jesus.yelo.sarrion@ulb.be

^{b)}Electronic mail: pedro.parra-rivas@uniroma1.it

ABSTRACT

We perform a systematic study of the temporal dynamics emerging in the asymmetrically driven dissipative Bose–Hubbard dimer model. This model successfully describes the nonlinear dynamics of photonic diatomic molecules in linearly coupled Kerr resonators coherently excited by a single laser beam. Such temporal dynamics may include self-pulsing oscillations, period doubled oscillatory states, chaotic dynamics, and spikes. We have thoroughly characterized such dynamical states, their origin, and their regions of stability by applying bifurcation analysis and dynamical system theory. This approach has allowed us to identify and classify the instabilities, which are responsible for the appearance of different types of temporal dynamics.

Published under an exclusive license by AIP Publishing. <https://doi.org/10.1063/5.0088597>

Self-sustained oscillations are common in nature and may emerge in a plethora of different systems in various scientific domains. By changing some of its parameters, a given system may undergo a number of instabilities where the oscillatory behavior can increase in complexity, eventually leading to chaotic dynamics. Of particular interest are nonlinear optical cavities in which these complex dynamical behaviors may arise. Applying dynamical systems theory, we characterize such dynamical regimes in the context of asymmetrically driven dissipative Bose–Hubbard dimers that can be realized with coupled Kerr resonators or circuit QED. Advances in these systems have a broad spectrum of applications in science and technology, which range from optically carried microwave signal generators for sensing and communication to spectroscopy, all-optical information processing, or quantum simulation.

I. INTRODUCTION

The emergence of self-sustained oscillations is commonly encountered in a variety of different fields ranging from chemistry

and biology to physics and engineering.^{1,2} Some examples include the Belousov–Zhabotinsky reaction,^{3,4} pulsation in Cepheid variable stars,² or the oscillatory biochemical dynamics responsible for the cell division cycle.⁵ In all these systems, the self-pulsing behavior emerges when varying a given parameter beyond a critical value, where time translation symmetry is broken. This oscillatory instability is known as a Hopf bifurcation^{6,7} and is key to understanding these dynamical phenomena. The self-sustained oscillations can evolve into much more complex dynamics. One example is chaos,⁸ which is present in different natural systems, including weather and climate, fluid turbulent flow,⁹ and chemical reactions,¹⁰ to cite a few.

Rich temporal dynamics, such as self-pulsing,^{11–17} period-doubling,¹⁸ and chaos,¹⁹ may also appear in optical systems. Recently, different works have focused on the dynamics of two coupled Kerr resonators. This system is commonly known as *driven dissipative photonic Bose–Hubbard dimer* (PBHD), in analogy with the open quantum boson system.²⁰ It has been recently exploited for optical frequency combs,^{21–23} microwave signal generation,^{24–26} or quantum-limited measurements.²⁷

Dissipative Bose–Hubbard dimers can be symmetrically (or anti-symmetrically) driven by equally exciting both coupled bosonic

modes or be asymmetrically driven. In most experiments, dissipative dimers are asymmetrically driven by exciting only one of the two bosonic modes,^{21,25–32} thus requiring less critical beam alignment³³ or avoiding precise control of the relative phase between the coherent excitations. Self-pulsing oscillations have been theoretically predicted to occur in asymmetrically driven PBHDs^{15,24} and were recently demonstrated with coupled microcavities²⁵ and fiber resonators.²⁶ In this latter work, we showed an excellent agreement between the experiments and the theoretical predictions from the canonical Bose–Hubbard dimer model. Still, coupled resonators may exhibit much richer dynamics ranging from chaos to spiking dynamics. These dynamics have been shown for two or more coupled cavities by direct numerical integration of the model.¹⁵ Period doubling cascade to chaotic behavior and similar complex dynamics have been analyzed theoretically by bifurcation analysis but this work was restricted to symmetrically driven dimers.^{34,35} However, the presence (symmetric case) or absence (asymmetric case) of a phase space mirror symmetry leads to important modifications of the phase space dynamics and bifurcation structure of the systems.

In this paper, following a bifurcation theory approach to dynamical systems, we present in a didactic manner a methodical study of the dynamics, stability, and bifurcation structure of asymmetrically driven dissipative PBHDs. The paper is organized as follows. In Sec. II, we introduce the driven dissipative PBHD model, and we describe some of its characteristics, the 4D dynamical system associated with it, and the methodological approach that we will follow. Section III focuses on the steady states of the system, analyzing their linear stability and steady bifurcations for two coupling regimes. After that, in Sec. IV, we perform a detailed bifurcation analysis of the previous coupling regimes, and we characterize the different dynamical scenarios. The origin of such dynamics is related to the presence of Hopf and homoclinic bifurcations. Later (see Sec. V), we study two homoclinic orbits of different types and present their main features. Section VI is devoted to elucidating the origin of the temporal chaos found in the system. Finally, we discuss our results and draw our conclusions in Sec. VII.

II. THE ASYMMETRICALLY DRIVEN DISSIPATIVE PHOTONIC BOSE–HUBBARD DIMER MODEL

Let us assume two coupled identical resonators, asymmetrically driven via the excitation of only one of the two resonators. The dynamics of such PBHD can be described by two coupled one-dimensional normalized Lugiato–Lefever equations²⁶

$$\begin{aligned} \frac{d\psi_1}{dt} &= [-1 + i(|\psi_1|^2 - \Delta)]\psi_1 + iC\psi_2 + S, \\ \frac{d\psi_2}{dt} &= [-1 + i(|\psi_2|^2 - \Delta)]\psi_2 + iC\psi_1. \end{aligned} \tag{1}$$

When considering coupled Kerr ring resonators, the normalization is as follows. The normalized time is $t = t' \kappa / T_R$, where t' is the laboratory time, T_R is the round-trip time, and κ is the cavity loss coefficient when uncoupled. The detuning from the closest (single cavity) resonances is $\Delta = \delta / \kappa = (m2\pi - \varphi) / \kappa$, where φ is the round-trip linear phase shift and m is an integer number. $C = \sqrt{\theta_{12}} / \kappa$, where θ_{12} is the transmission coefficient of the coupler between the cavities. Finally, $\psi_j = A_j \sqrt{\gamma L / \kappa}$ ($j = 1, 2$) and $S = i \sqrt{P_p \gamma L \theta_p / \kappa^3}$, where A_j

are the field amplitudes normalized such that the intracavity powers (expressed in watts) are given by $|A_j|^2 = P_j$. P_p is the driving power, θ_p is the transmission coefficient of the input coupler, γ is the nonlinear parameter of the waveguide and L is the length of the resonators.

To study this system, we apply two different procedures: the direct numerical integration of Eq. (1), using a Runge–Kutta–Fehlberg algorithm, and the numerical path-continuation^{36,37} of the different states of the system using the open-source software continuation package AUTO-07p.³⁸ This last approach allows us to characterize the bifurcation structure and stability of the different static and periodic dynamical states as a function of the parameters of the system. For the periodic states, Floquet analysis is applied.³⁹

To perform numerical parameter continuation, it is convenient to recast the complex dynamical system (1) into the 4D system,

$$\begin{aligned} \frac{du_1}{dt} &= -u_1 - (u_1^2 + v_1^2 - \Delta)v_1 - Cv_2 + S, \\ \frac{dv_1}{dt} &= -v_1 + (u_1^2 + v_1^2 - \Delta)u_1 + Cu_2, \\ \frac{du_2}{dt} &= -u_2 - (u_2^2 + v_2^2 - \Delta)v_2 - Cv_1, \\ \frac{dv_2}{dt} &= -v_2 + (u_2^2 + v_2^2 - \Delta)u_2 + Cu_1, \end{aligned} \tag{2}$$

where $\psi_j = u_j + iv_j$ for $j = 1, 2$. As control parameters, we consider the pump field S , the coupling constant C , and the phase detuning Δ .

This system supports self-pulsing dynamics, i.e., periodic oscillations in time, as schematically shown in Fig. 1(b). Through the modification of suitable parameters, these oscillations can suffer different transitions, leading to more complex dynamics. One example of such complexity, corresponding to chaos, is depicted in Fig. 1(c). In what follows, we will unveil the features of these states and the transition that they may encounter.

III. STEADY STATES, LINEAR STABILITY, AND THEIR PHASE DIAGRAM

The steady states of the system correspond to the fixed points or equilibria $\psi_e = (\psi_1^e, \psi_2^e) = (u_1^e, v_1^e, u_2^e, v_2^e)$ of Eq. (1), such that $d\psi_j/dt = 0$. They are solution of the algebraic system

$$\begin{aligned} [-1 + i(|\psi_1|^2 - \Delta)]\psi_1 + iC\psi_2 + S, \\ [-1 + i(|\psi_2|^2 - \Delta)]\psi_2 + iC\psi_1 = 0, \end{aligned} \tag{3}$$

which leads to

$$\begin{aligned} |\psi_1|^2 + (|\psi_1|^2 - \Delta)^2 |\psi_1|^2 - C^2 |\psi_2|^2 - S^2 + 2CSv_2 = 0, \\ |\psi_2|^2 + (|\psi_2|^2 - \Delta)^2 |\psi_2|^2 - C^2 |\psi_1|^2 = 0. \end{aligned} \tag{4}$$

The linear stability of these points is obtained from the local dynamics of (2) around ψ_e , which is solely determined by the eigenvalues λ of the Jacobian \mathcal{J} of the system at that point. The complicated form of Eq. (4) prevents the possibility of extracting an analytical expression of the eigenvalues of the system. However, the equilibria

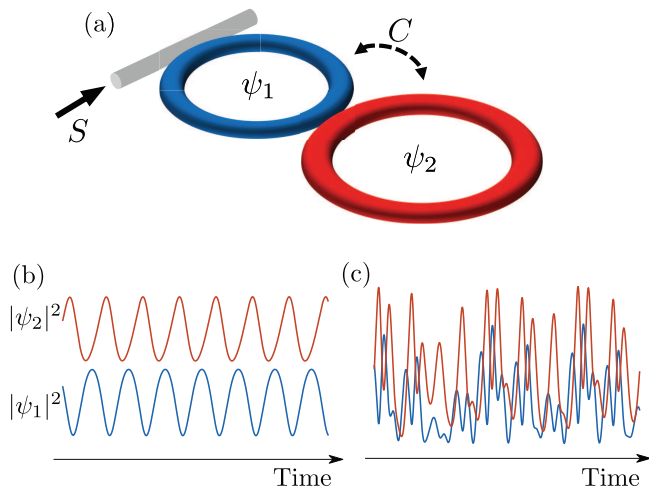


FIG. 1. (a) Schematic view of an asymmetrically driven dissipative PBHD. C represents the coupling between cavities and S the driving field. (b) Temporal traces of the cavity powers $|\psi_{1,2}|^2$ in a self-pulsing regime. (c) Same as in (b) but in a chaotic dynamics regime.

and their stability can be easily computed numerically through the path-continuation algorithm.^{36,37}

When two cavities are coupled, each resonance splits into two peaks. These peaks correspond to the excitation of the hybridized modes, often called the antibonding-like (AB) ($\Delta < 0$) and the bonding-like (B) ($\Delta > 0$) modes of the photonic dimer.²⁶ The AB and B resonances are marked in Figs. 2(i) and 2(vi). The detuning separation between them is equal to $2C$ and can, thus, be freely adjusted through the cavity coupling strength. Owing to the asymmetric driving, the two resonances can be excited when scanning the detuning. In stark contrast, at low power, a symmetric driving can only excite the linear symmetric resonance.

In this study, we consider two main dynamical regimes corresponding to the *weakly coupled* scenario ($C = 1.5$) for which the splitting is only slightly larger than the resonance width, and the *strongly coupled* scenario ($C = 5$), showing a much larger peak separation. Hereafter, we refer to them as WC and SC regimes, respectively. The coupling constant that we consider in the WC regime is similar to the experimental value of our previous work,²⁶ while the coupling in the SC regime can typically be achieved in integrated photonic dimers or circuit QED. Note that in the latter case, while the encountered dynamics look similar, they are much richer and the bifurcation diagram is more complex. In what follows, we study these two regimes separately. Their steady-state bifurcation structure is summarized in the diagrams plotted in Fig. 2.

A. Steady states in the weakly coupled regime

Figure 2(a) shows the steady-state phase diagram in the (Δ, S) -parameter space for $C = 1.5$. Slices of such diagram, for increasing values of S , are depicted in Figs. 2(i)–2(v) where the normalized powers $|\psi_{1,2}|^2$ are plotted against Δ . The linear stability of these

states is marked using solid (dashed) lines for stable (unstable) equilibria, and only steady-state bifurcations are labeled.

The two resonances partially overlap in the WC regime as can be seen for $S = 1$ [see Fig. 2(i)] for which the system is still close to the linear regime. At this driving level, the resonances are only slightly asymmetric, a single equilibrium exists for each given value of Δ and it is linearly stable. Note that, in the whole region of detuning, $|\psi_1(\Delta)| \neq |\psi_2(\Delta)|$ except in some particular points where the curves intersect. This is a feature induced by the asymmetric driving and the weak coupling. In the symmetric case, naturally, the power in each ring is equal ($|\psi_1|^2 = |\psi_2|^2$), due to the mirror invariance. Hence, asymmetric states (i.e., $|\psi_1(\Delta)| \neq |\psi_2(\Delta)|$) could only appear through a symmetry breaking pitchfork bifurcation,³⁵ as recently experimentally demonstrated with photonic crystal nanocavities.³³

Increasing S [see Fig. 2(ii) for $S = 2$], the asymmetry between the resonances increases, yielding a larger right resonance to the detriment of the left one. The right resonance undergoes a cusp or hysteresis bifurcation C_1 , where a pair of folds, or turning points, are created, leading to the tilted shape.³⁹ These folds correspond to saddle-node bifurcations that we label SN_1^{lr} . At these bifurcations, a stable node equilibrium and an unstable saddle collide and disappear. This transition leads to the coexistence of three different equilibria $\psi_e^{\alpha,\beta,\gamma}$, where ψ_e^α and ψ_e^β are stable nodes, whereas ψ_e^γ is a saddle.³⁹ The separation in Δ between SN_1^{lr} and SN_1^{lr} defines the coexistence region CR_1 (see light orange area).

Further increasing S , both resonances tilt to the right due to the effect of the nonlinearity and two new cusp bifurcations occur [see Figs. 2(a) and 2(iii) for $S = 3$]: C_2 on the right resonance, and C_3 on the left one. In C_2 , SN_2^{lr} are created. This pair of bifurcations leads to the equilibria ψ_e^δ and ψ_e^ϵ (see close-up view), which are both unstable and coexist in CR_2 . C_3 creates SN_3^{lr} , and the two new equilibria ψ_e^μ and ψ_e^ν associated with the left resonance appear. Between SN_3^{lr} , the bistability region CR_3 is created.

In Fig. 2(iv), we plot the bifurcation diagram for $S = 4$. For this value, the tilting of the resonance is much more prominent, and the bistability interval between ψ_e^α and ψ_e^γ has increased considerably. For increasing values of S , the separation between the pairs SN_1^{lr} , SN_2^{lr} , and SN_3^{lr} increases [see Fig. 2(a)], and a *multi-coexistence region* appears between SN_1^{lr} and SN_3^{lr} that we label MC_{1-3} . An example of this situation is depicted in Fig. 2(v) for $S = 7$. We can see how the overlapping between both resonances leads to tristability,⁴⁰ a regime that is absent in the symmetrically driven scenario.³⁵

B. Steady states in the strongly coupled regime

Let us now focus on a scenario with a higher coupling and fix $C = 5$. Figure 2(b) shows the phase diagram for that coupling, and Figs. 2(vi)–2(x) show the bifurcation diagrams for some relevant values of S . In the linear regime, the two resonances are now well separated. At $S = 1$, they are still almost symmetric [see Fig. 2(vi)].

Increasing S , the system encounters C_1 and C_3 almost simultaneously, where the pairs SN_1^{lr} and SN_3^{lr} , together with the equilibria $\psi_e^{\alpha,\dots,\epsilon}$ are created as seen in Fig. 2(b). These bifurcations define the coexistence regions CR_1 and CR_3 . An example of this configuration is plotted in Fig. 2(vii) for $S = 3$, where different equilibria are

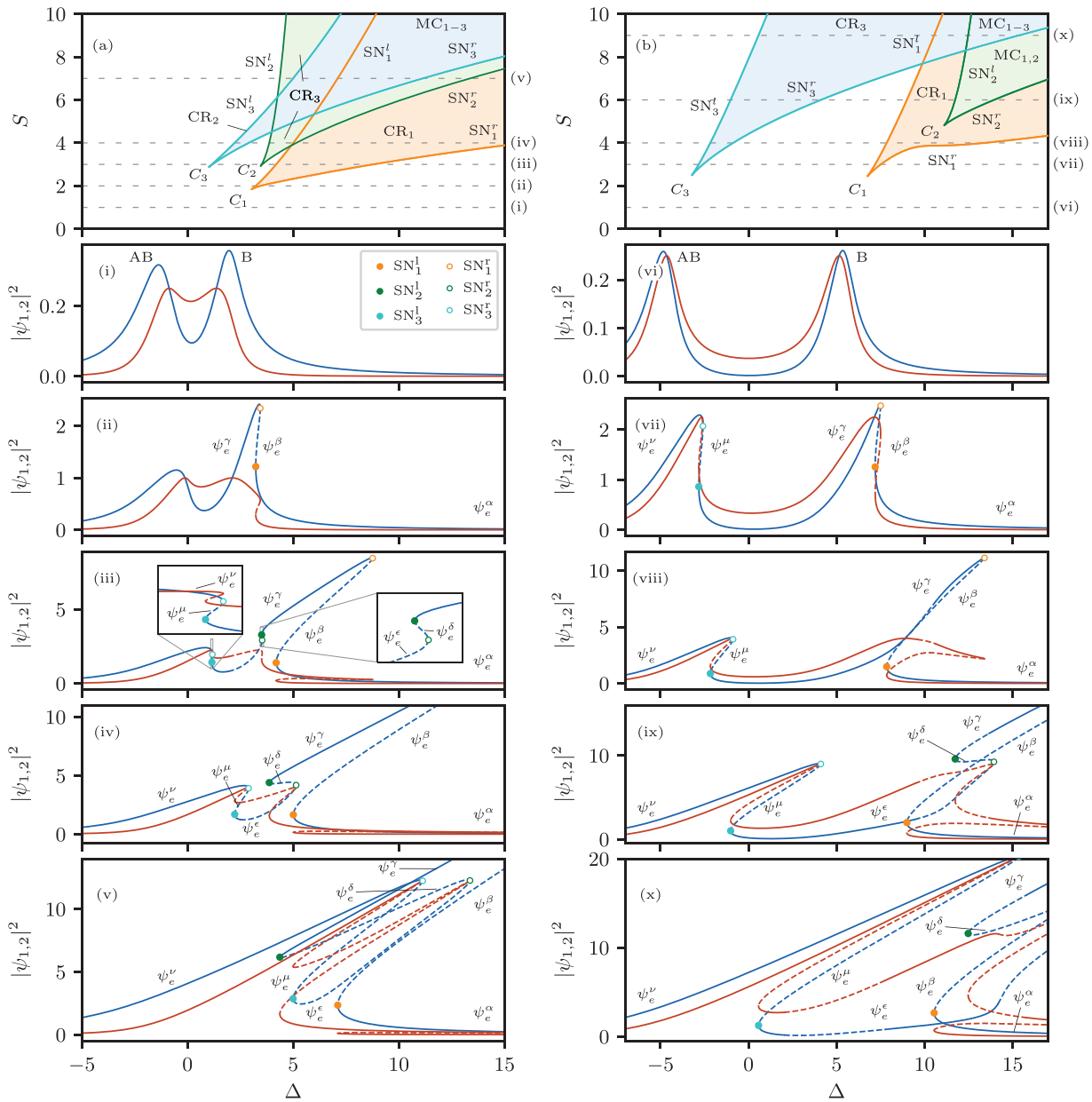


FIG. 2. Steady-state phase diagrams in the weakly and strongly coupled regimes. (a) shows the (Δ, S) -phase diagram for $C = 1.5$. The bifurcation diagrams shown in panels (i)–(iv) correspond to slices of constant S [see dashed horizontal lines in (a)]. They represent the powers $|\psi_1|^2$ (blue) and $|\psi_2|^2$ (red) as a function of Δ . From top to bottom, the values are $S = 1, 2, 3, 4$, and 7 . (b) shows the (Δ, S) -phase diagram for $C = 5$. Panels (v)–(x) are slices of panel (b) for the constant values $S = 1, 3, 4, 6$, and 9 (from top to bottom). Solid and dashed lines represent stable and unstable equilibria (ψ_e^i), respectively. In (a) and (b), different coexistence regions (CR_i) and multi-coexistence regions (MC_i) are depicted as well as the static bifurcations of the equilibria: saddle-node $SN_i^{l,r}$ and cusp C_i .

depicted. For this value of S , the resonance already tilts slightly to the right.

The system undergoes an interesting modification for $S = 4$ as shown in Fig. 2(viii). For this driving value, the right resonance enlarges due to its merging with an isola (not shown here). The

merging occurs through a necking bifurcation,⁴¹ similarly to the one illustrated in our previous work.²⁶

Moving up in Fig. 2(b), C_2 occurs and $SN_2^{l,r}$ are created. After this point, the configuration is like the one depicted in Fig. 2(ix) for $S = 6$. For this value of S , SN_1^l and SN_1^r are

far apart, and the right resonance extends to larger values of Δ .

For $S = 9$ [see Fig. 2(x)], the left resonance has grown significantly as SN_3^r overpasses SN_1^l and SN_2^l . At this stage, a tristable regime appears. Tristability persists for even larger values of S , where an effective single resonance can emerge similarly to the case shown in Fig. 2(v). We can identify two main regions of multi-coexistence that are labeled $\text{MC}_{1,2}$ and MC_{1-3} .

IV. DYNAMICAL REGIMES AND BIFURCATION STRUCTURE

In Sec. III, we focused on the steady-state equilibria and their steady bifurcations. As previously stated, self-pulsing oscillations and chaos may emerge in the system [see Figs. 1(b) and 1(c)]. In this section, we expand the previous analysis by studying the dynamical behavior of the system and present a systematic analysis of the bifurcation structure associated with such states in the WC and SC regimes.

A. Dynamics in the weakly coupled regime

The phase diagram shown at the top of Fig. 3 summarizes the main dynamical regimes and bifurcation lines of the system for $C = 1.5$. To understand such a diagram, we slice it as shown by the horizontal and vertical dashed lines. Each of these lines corresponds to one of the bifurcation diagrams shown below. The slices with constant S are plotted in Figs. 3(i)–3(iii), whereas those with constant Δ are depicted in Figs. 3(iv)–3(vi).

Figure 3(i) shows a close-up view of Fig. 2(ii) around the bistability region between ψ_e^α and ψ_e^γ for $S = 2$. Upon increase of S , the Hopf bifurcation (H) line plotted in Fig. 3(a) is crossed, and the system enters a self-pulsing regime (see red shadowed region) characterized by single-period oscillations like those shown in Fig. 1(b). An example in this configuration is plotted in Fig. 3(ii) for $S = 2.5$, where H is crossed at two points H^a and H^b . The periodic oscillations emerge supercritically from H^a and with small amplitude from the left. The maximum and minimum of the oscillation are represented using red solid lines. Increasing Δ , the oscillation amplitude grows until suddenly it dies out at H^b on the right. This dramatic change of the oscillation amplitude in phase space is called *canard explosion*,⁴² and is related to type-II excitability.^{43–45}

For $S = 3.5$, the situation is shown in Fig. 3(iii). For this value, the equilibria ψ_e^δ , ψ_e^ϵ , and ψ_e^μ , ψ_e^ν , coexist. Furthermore, periodic oscillations persist. On the left, they still emerge from H^a . On the right, however, they die in a *homoclinic* (Hom) bifurcation,^{7,46} while only steady states persist for larger values of Δ . In the gray region shown in Fig. 3(a), just after crossing the Hom line, oscillatory states are absent.

The homoclinic bifurcations are global bifurcations related to the collision of a limit cycle (i.e., a periodic orbit Γ) with an equilibrium, and are characterized by the divergence of the cycle's period.⁴⁶ At the bifurcation point, the limit cycle Γ becomes a homoclinic orbit γ , i.e., a trajectory in the phase space which is bi-asymptotic to the equilibrium. This bifurcation is associated with type-I excitability.⁴³

In the phase diagram of Fig. 3(a), the Hom bifurcation corresponds to the black solid line. To track numerically this line in the (Δ, S) -parameter space, we have used the homoclinic continuation HOMCONT extension of AUTO-07p.⁴⁷ We will focus our attention on this type of bifurcations in Sec. V.

We can also analyze the (Δ, S) -phase diagram considering slices of constant Δ . The resulting bifurcation diagrams are shown in Figs. 3(iv)–3(vi), where $|\psi_1|^2$ is plotted as a function of S . In Fig. 3(iv) [$\Delta = 2$], bistability exists between SN_3^l and SN_3^r , and the limit cycle Γ emerges and dies at H^a and H^b , respectively. For this slice, bistability exists between ψ_e^ϵ and ψ_e^ν .

Increasing Δ [see Fig. 3(v) for $\Delta = 3$], the bistability interval is now bound by H^b and SN_3^r . Γ increases drastically its amplitude and undergoes several secondary bifurcations such as saddle-node bifurcation of periodic orbits (SNP), also known as fold of cycles, and period-doubling bifurcations (PD).^{39,48} For clarity, we do not plot these bifurcation lines in the phase diagram of Fig. 2(a). The presence of a PD may suggest the existence of chaotic dynamics emerging from a period-doubling cascade.⁸ We will analyze the chaotic dynamics of this system in Sec. VI.

In Fig. 3(vi) [$\Delta = 4$], we plot the bifurcation diagram after the occurrence of C_2 and C_1 . The bistability between H^b and SN_3^r reduces drastically (see close-up view), and the pair of bifurcations $\text{SN}_2^{l,r}$ and $\text{SN}_1^{l,r}$ appear. Between the last two bifurcations, a new bistability range emerges, where ψ_e^α and ψ_e^γ coexist. This slice cuts Hom into three different points that we label $\text{Hom}^{a,b,c}$, respectively. Periodic oscillations exist between Hom^a and Hom^b , and between Hom^c and H^b .

The region in-between the H and Hom lines in the (Δ, S) -parameter space [see the red shadowed area in Fig. 3(a)] is the dynamical region of the system where self-pulsing and other dynamical states (e.g., chaos) may emerge.

The H and Hom bifurcations arise from a pair of codimension-two Takens–Bodganov (TB) bifurcations,^{6,39} which occur at SN_2^l and SN_2^r . For the range of parameters considered here, we only observe TB_1 [see a close-up view in Fig. 3(a)]. At this bifurcation, the linearized dynamics of the system has two zero eigenvalues $\lambda_{1,2} = 0$ (with algebraic multiplicity 2); for this reason, it is also known as a double zero bifurcation.⁶ The periodic oscillations arise from this point with an infinite period, which becomes finite as H separates from Hom.

B. Dynamics in the strongly coupled regime

Let us now analyze the bifurcation structure of the system in the SC regime. The (Δ, S) -phase diagram plotted in Fig. 4(a) summarizes the main dynamical regions of the system for $C = 5$. One of the main differences is the presence of two distinct, but connected, single-period oscillatory regimes (see red shadowed regions bounded by H_1 and H_2), which were fused for smaller values of C [see phase diagram in Fig. 3(a)]. The steady-state bifurcations (i.e., the saddle-nodes) are the same as those already plotted in Fig. 2(b). In addition to the two Hopf bifurcations H_1 and H_2 , two $\text{SNP}_{1,7}$, several period-doubling bifurcations PD_{1-3} , and two homoclinic bifurcations $\text{Hom}_{1,2}$ are drawn.

To understand this diagram, we take several slices at constant S . The corresponding bifurcation diagrams are shown in

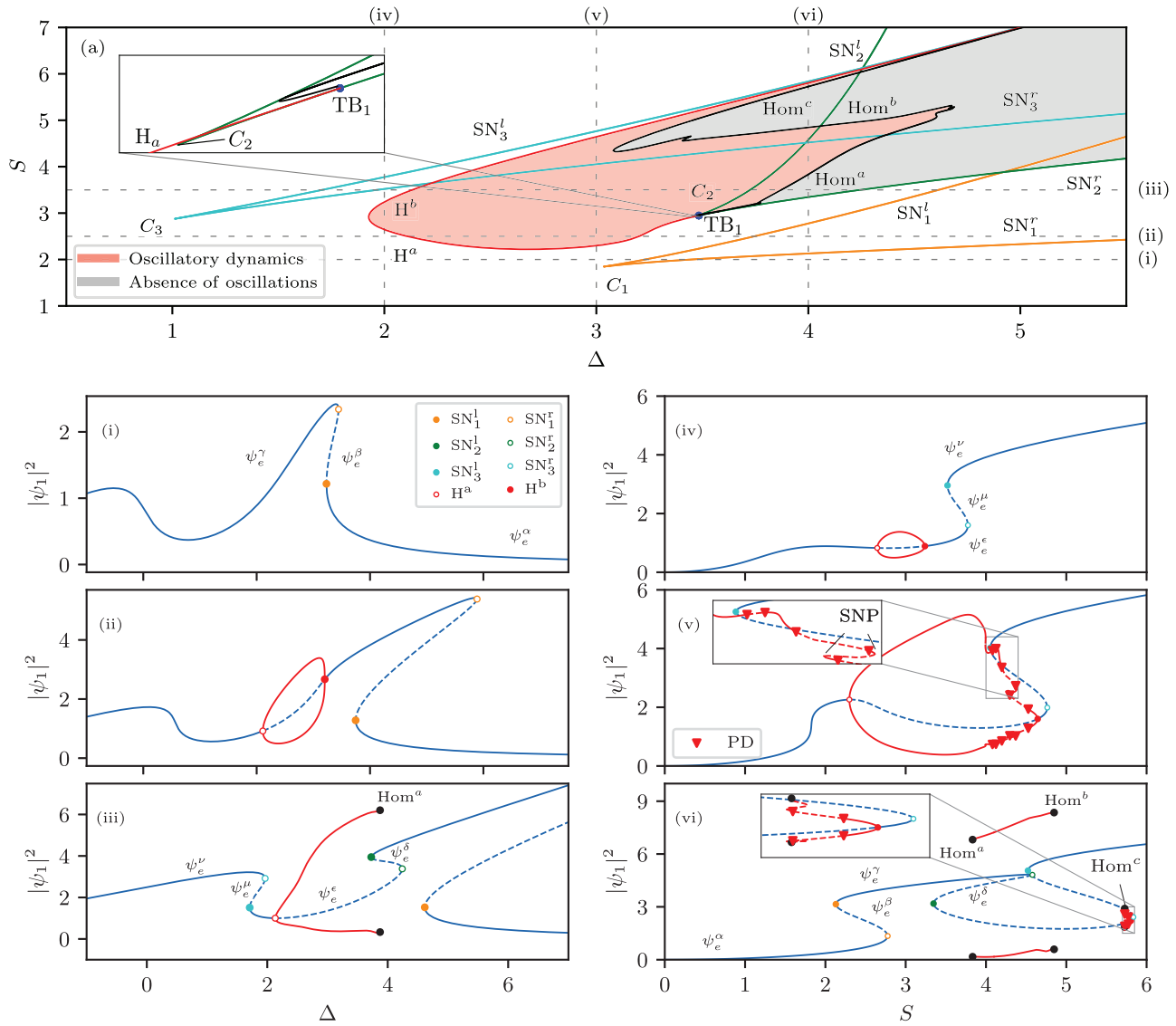


FIG. 3. (a) Phase diagram in the (Δ, S) -parameter space for $C = 1.5$ showing the main dynamical regions and bifurcations of the system: saddle-node of the steady state SN_1^r , cusp C_i , Hopf $H^{a,b}$, saddle-node of periodic oscillatory states SNP, homoclinic $Hom^{a,b}$, and Takens–Bogdanov TB_j . The red shadowed region corresponds to self-pulsing dynamics. The vertical and horizontal dashed lines correspond to the bifurcation diagrams shown in panels (i)–(iii) for constant S ($= 2, 2.5$, and 3.5), and panels (iv)–(vi) for constant Δ ($= 2, 3$, and 4). Stable and unstable equilibria (ψ_e^i) are plotted with solid and dashed lines, respectively. The red lines represent the maxima and minima of the periodic oscillations.

Figs. 4(i)–4(v). Let us first analyze the bifurcation structure and dynamics around the right nonlinear resonance emerging from C_1 . The modification of the dynamical scenario around this resonance is depicted in **Figs. 4(i)–4(iv)**.

The diagram shown in **Fig. 4(i)** [$S = 4.5$] intersects H_2 at two points, labeled H_2^a , from where periodic oscillations arise. Due to the complexity of this scenario, we have used different colors for each of the limit cycles. In red, we plot the maximum and minimum

of the oscillation arising from H_2^a and in orange the one emerging from H_2^b . The linear stability of these limit cycles is depicted with solid lines for stable states and dashed lines for the unstable ones. The limit cycle arising from H_2^a , hereafter Γ_a , undergoes a pair of secondary $SN_{1,2}$. For simplicity, we only plot $SN_{1,2}$ in **Fig. 4(a)**. Increasing Δ , Γ_a encounters the homoclinic bifurcation Hom_1^a where it is destroyed. The limit cycle originating from H_2^b , however, quickly undergoes a PD_1 bifurcation when decreasing Δ .

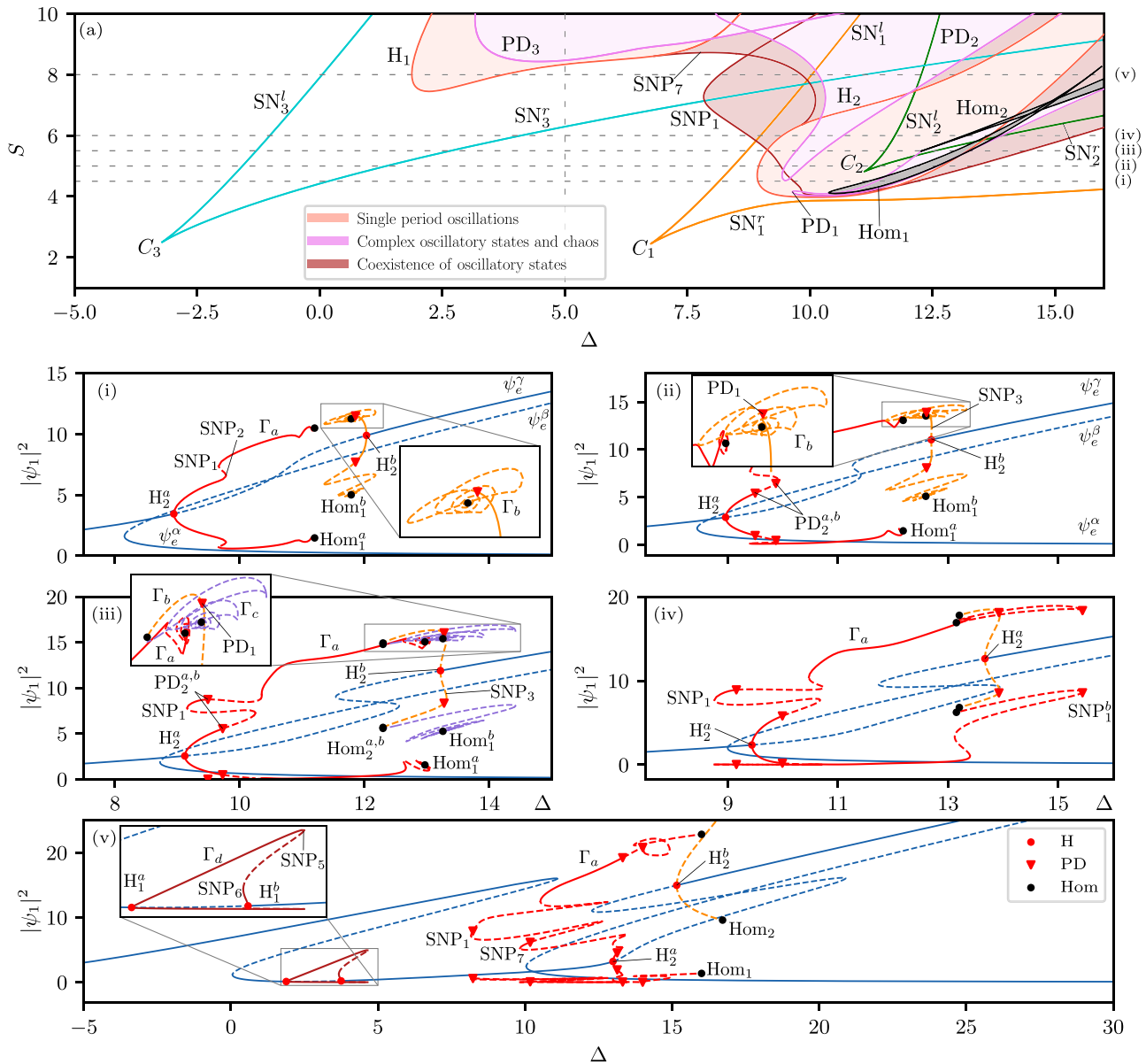


FIG. 4. Bifurcation structure for $C = 5$. (a) shows the phase diagram in the (Δ, S) -parameter space, which illustrates the different dynamical regions and main bifurcations of the system: saddle-node of the steady-state $SN_i^{r,s}$, Hopf $H_{1,2}^{a,b}$, period-doubling $PD_i^{a,b}$, saddle-node of periodic oscillatory states SNP_i , and homoclinic $Hom_{1,2}^{a,b}$. The horizontal dashed lines correspond to the bifurcation diagrams shown below, where $|\psi_1|^2$ is plotted as a function of Δ for $S = 4.5$ (i), 5 (ii), 5.5 (iii), 6 (iv), and 8 (v). The vertical dashed line corresponds to the bifurcation diagram shown in Fig. 8(a). In diagrams (i)–(v), solid (dashed) lines represent stable (unstable) equilibria (ψ_δ) and limit cycles (Γ).

We label this oscillatory state Γ_b . Eventually, the extrema of Γ_b develop a spiral structure which collapses to the Hom_1^b (see close-up view). This spiral behavior is typical of one type of homoclinic bifurcation.³⁴ Between Hom_1^a and Hom_1^b , the only attractor of the system is ψ_e^α .

With increasing S [see Fig. 4(a)], the period-doubling bifurcation line PD_2 appears, and SN_2^r are created at C_2 . The bifurcation

diagram in this regime is as shown in Fig. 4(ii) for $S = 5$. For this value, PD_2 is sliced in two points, namely, $PD_2^{a,b}$. With increasing Δ , Γ_a increases its amplitude and eventually starts to spiral around Hom_1^a , where it is finally destroyed (see close-up view). Γ_b now emerges from H_2^b subcritically and stabilizes at SNP_3 before losing stability in PD_1 . Once this point is crossed, Γ_b describes a large spiral, before dying at Hom_1^b .

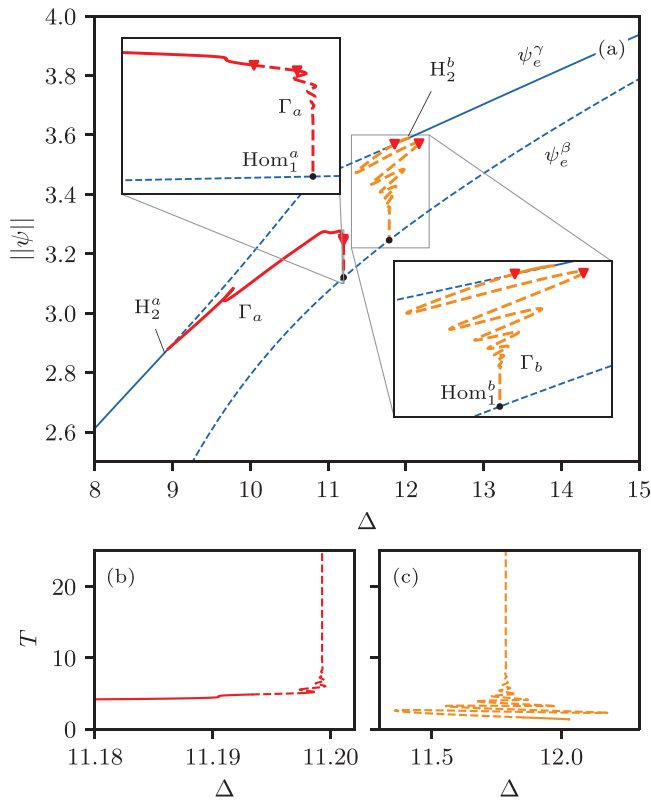


FIG. 5. Shilnikov homoclinic bifurcations for $C = 5$ and $S = 4.5$. (a) Close-up view of the diagram shown in Fig. 4(i) around $\text{Hom}_1^{a,b}$. Here, we plot $\|\psi\|$ as a function of Δ . (b) shows the divergence of the period T of Γ_a at Hom_1^a and (c) the damped oscillatory modification of the period of Γ_b with Δ around Hom_1^b . See Fig. 4 for the definition of the labels.

Figure 4(iii) shows the modification of the bifurcation diagram for $S = 5.5$. As $\text{SNP}_{1,2}$ are further apart, we can see that stable oscillations of different amplitudes coexist in a narrow Δ interval in-between SNP_1 and the closest PD_2 point. However, the main difference is seen in the right part of the diagram. Γ_b emerges subcritically from H_2^b (see orange curve) and becomes stable at SNP_3 , just before being destabilized at PD_1 once more. However, in contrast to Fig. 4(ii), Γ_b does not describe a spiral around Hom_2^a but approaches that point monotonically. Very close to Hom_2^a , the cycle is created again at Hom_1^b , leading to the purple unstable curve Γ_c . This cycle is mainly unstable and spirals around Hom_1^b , where it is finally destroyed. A detailed study of this configuration is presented in Sec. V (see Fig. 5).

The bifurcation structure is very similar for $S = 6$ [see Fig. 4(iv)], with larger separations between the different saddle-node bifurcations. For simplicity, we have omitted the solution branches associated with Γ_c . For this value of S , $\text{Hom}_1^{a,b}$ occurs near one another. From a stability perspective, everything is equivalent to the case for $S = 5.5$.

We have discussed so far the bifurcation structure of the dynamical states emerging from H_2 (i.e., around the right resonance) as this bifurcation is first encountered when S is increased. However, for S larger than ≈ 7.5 , complex nonlinear dynamics also occur around the left nonlinear resonance. Figure 4(v) illustrates a slice of Fig. 4(a) for $S = 8$, where both resonances are plotted. For this value, the bifurcation structure of the oscillations around the tilted right resonance becomes much more complex. Regarding the tilted left one, a new oscillatory state Γ_d emerges supercritically from H_1^a . Γ_d increases its amplitude with Δ and becomes unstable at SNP_5 . From H_1^b , the periodic orbit also emerges supercritically, although it undergoes SNP_6 where it becomes unstable. These oscillations correspond to the instability mechanism reported in Refs. 25 and 49 in which the nonlinearity shifts the resonances so as to allow for a resonant four-wave-mixing process with signal and idler photons, respectively, on the bonding- and antibonding-like mode of the dimer. Conversely, the parametric instability originating from H_2 involves signal and idler photons in the same mode (see the supplemental material of Ref. 26).

From each PD bifurcation, a period-doubling cascade can be triggered, potentially leading to chaotic dynamics.⁸ Period doubled states and chaotic ones will be analyzed in detail in Sec. VI.

For $C = 5$, neither the Hopf nor the homoclinic bifurcations emerge from TB points, in contrast to the case in Sec. III for $C = 1.5$. Regarding $H_{1,2}$, we have found that they extend to large values of Δ and S [far from the range of validity of the mean-field Eq. (1)⁵⁰], and no signs have been found about their relation with TB points. Similarly, we have established that Hom_1 forms a close loop in the parameter space, and, thus, they are detached from any codimension-two point.

V. HOMOCLINIC BIFURCATIONS

In Sec. IV, we have found that for some ranges of parameters the periodic oscillations emerging at Hopf bifurcations die out in global homoclinic bifurcations. These bifurcations take place when a limit cycle Γ collides with an unstable (hyperbolic) equilibrium for some set of parameters. As the cycle approaches the unstable equilibrium, its period drastically grows, diverging at Hom .^{7,39} At this point, the periodic solution Γ becomes a homoclinic orbit γ , i.e., a closed trajectory linking the unstable equilibrium with itself. Depending on the nature of such equilibrium, different types of Hom bifurcations take place.^{7,51} In our system, we have identified two types corresponding to the following conditions:

- When the leading eigenvalues $\lambda_{1,2}$ of the Jacobian \mathcal{J} are real (i.e., $\lambda_{s,u} = a_{s,u} \in \mathbb{R}$) such that $a_s < 0 < a_u$, the Hom orbit γ is biasymptotic to a saddle equilibrium, and the Hom bifurcation is commonly called *saddle-loop* Hom bifurcation.⁴³
- If the leading eigenvalues of \mathcal{J} are one real and one complex conjugate pair (i.e., $\lambda_s = a_s \pm i\omega_s$ and $\lambda_u = a_u$), with $a_s < 0 < a_u$ and $\omega_s > 0$, the Hom orbit is biasymptotic to a saddle-focus (SF) equilibrium, and the bifurcation is known as saddle-focus Hom bifurcation or *Shilnikov* bifurcation.⁴⁶ A relevant parameter describing the nature of these points is the *saddle-index* quantity,⁷

$$\delta \equiv -\text{Re}[\lambda_s]/\lambda_u. \tag{5}$$

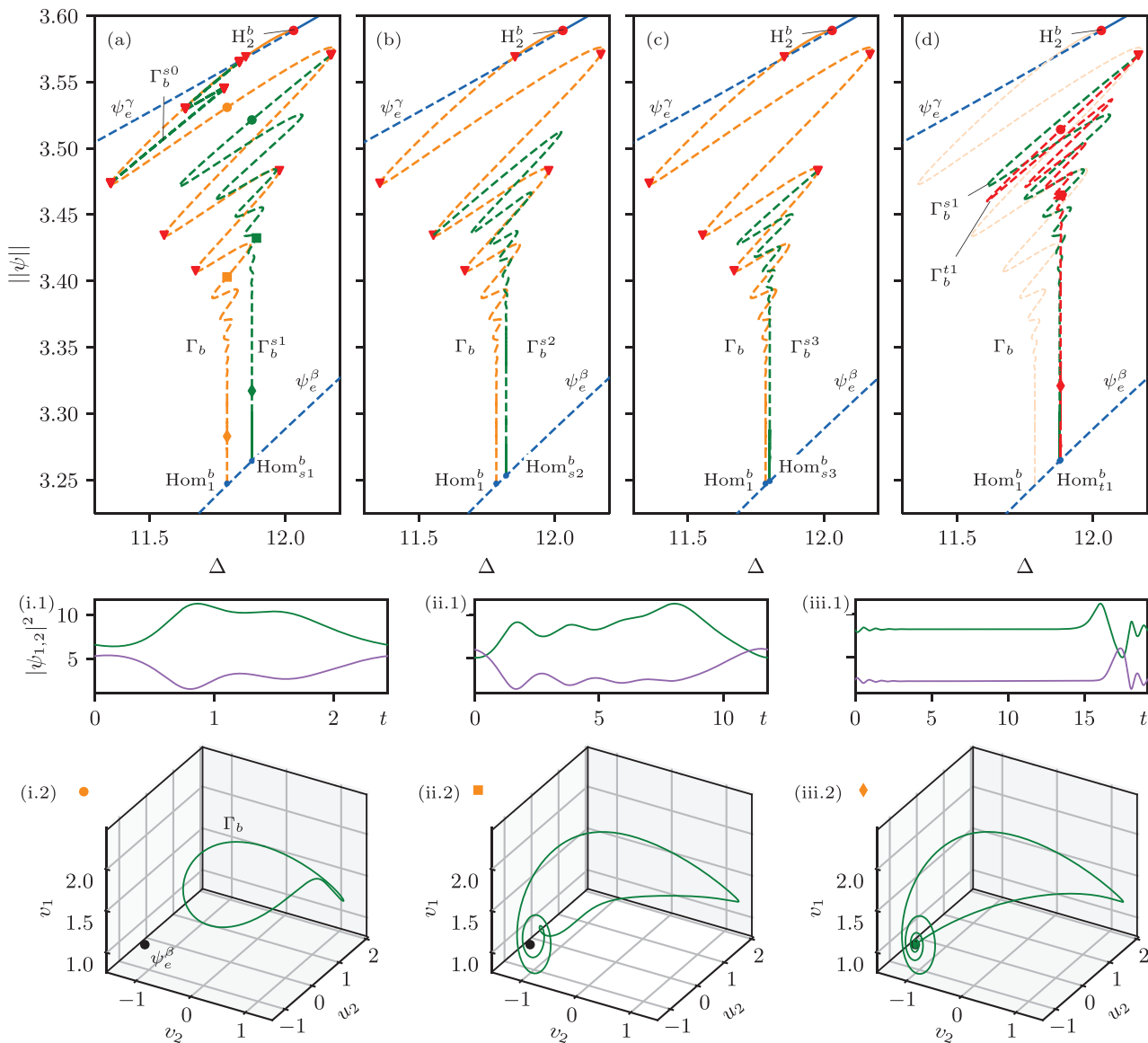


FIG. 6. Bifurcation diagram of the principal and subsidiary periodic orbits close to Hom_1^b for $C = 5$ and $S = 4.5$. (a) shows the bifurcation curve associated with the principal orbit Γ_b emerging from H_2^b and dying at Hom_1^b . Two subsidiary branches Γ_b^{s0} and Γ_b^{s1} are also plotted. Γ_b^{s1} connects with ψ_e^β at Hom_{s1}^b . (b) shows the principal orbit Γ_b and the subsidiary curve arising from the fourth PD bifurcation. We label with orbits and its bifurcation curve Γ_b^{s2} . In (c), we plot Γ_b and another subsidiary orbit Γ_b^{s3} , which dies at Hom_{s3}^b . (d) shows the subsidiary curve and Γ_b^{s1} and the tertiary oscillatory state Γ_b^{t1} arising from it. The modification of the oscillatory state Γ_b descending its bifurcation curve [see orange \bullet , \blacksquare , \blacklozenge in (a)] is depicted in panels (i)–(iii), where the temporal trace and 3D attractors are depicted.

When $\delta > 1$, the saddle-focus homoclinic orbit is said to be *tame*⁴⁶ and the dynamics are essentially the same as in the saddle-loop case. In contrast, when $\delta < 1$, the homoclinic orbit is called *wild* and the dynamics of the system around it is richer. In particular, there is an infinite number of SNP and period-doubling bifurcations in any parameter interval containing the bifurcation.^{7,46,48}

Let us analyze these bifurcations in our case.

A. Saddle-focus (Shilnikov) homoclinic bifurcation

Most of the homoclinic bifurcations and orbits appearing in our system are of the Shilnikov type. The bifurcation diagram plotted in Fig. 5(a) shows the appearance of these bifurcations for $C = 5$

TABLE I. Features and relevant information about the wild Shilnikov homoclinic bifurcations plotted in Fig. 6. SF stands for saddle-focus equilibrium, λ_s represents the stable eigenvalues, λ_u is the unstable real eigenvalue, and δ is the saddle-index associated with the homoclinic bifurcation.

Label	ψ_e -type	Δ	λ_u	λ_s	δ
Hom_1^b	SF	11.7857	2.4078	$-1 - i7.9829$	0.4153
Hom_{s1}^b	SF	11.8769	2.4282	$-1 - i8.0693$	0.4118
Hom_{s2}^b	SF	11.8216	2.4159	$-1 - i8.0166$	0.4139
Hom_{s3}^b	SF	11.8009	2.4113	$-1 - i7.9971$	0.4147
Hom_{t1}^b	SF	11.8804	2.4289	$-1 - i8.0727$	0.4116

and $S = 4.5$. It consists of a close-up view of the diagram shown in Fig. 4(i). For more clarity, we plot the L_2 -norm as

$$\|\psi\| \equiv \sqrt{T^{-1} \int_0^T (|\psi_1(t)|^2 + |\psi_2(t)|^2) dt}, \quad (6)$$

as a function of Δ , where T is the period of the oscillatory state. This allows us to better visualize the occurrence of different Hom bifurcations.

Let us first take a look at the self-pulsing state Γ_b emerging from H_2^b . Soon after its birth, Γ_b undergoes a first PD bifurcation (see the red triangle), and its norm $\|\psi\|$ changes in a damped oscillatory fashion while approaching asymptotically Hom_1^b [see Fig. 5(a)]. This structure corresponds to the spiral shown in the inset of Fig. 4(i), and each fold to an SNP. All along this curve, the period of Γ_b increases as it approaches Hom_1^b , and in doing so, it describes the damped oscillatory curve in Δ plotted in Fig. 5(c). We refer to this state Γ_b as the *primary periodic orbit*.⁴⁸

In Fig. 6(a), we plot the bifurcation curve associated with the principal orbit Γ_b . Its change along such a curve is depicted in Figs. 6(i)–6(iii). In Fig. 6(i.1) we show the temporal trace of Γ_b during one oscillatory period, and in Fig. 6(i.2), its 3D representation in the phase subspace $\{(v_2, u_2, v_1)\}$.

Moving down along this diagram, the period T of Γ_b increases [see Fig. 6(ii.1)], while the periodic attractor approaches the saddle-focus equilibrium ψ_e^β . In doing so, the periodic orbit temporarily follows the flow around ψ_e^β , leading to the almost spiral-like trajectory shown in Fig. 6(ii.2). Close to Hom_1^b , the periodic orbit looks like the one shown in Fig. 6(iii), where the oscillatory period has considerably increased, and where the orbit describes a spiral trajectory around ψ_e^β . The behavior of the trajectory around this point follows the unstable and stable manifolds of the saddle-focus (SF) equilibrium, being the latter one, responsible for the oscillatory tail shown in its temporal trace.

Approaching Hom_1^b , the period of Γ_b tends to infinity, and at that point, Γ_b collides with the SF equilibrium ψ_e^β , leading to the formation of the wild Shilnikov homoclinic orbit γ_b . This homoclinic orbit is very similar to the periodic orbit shown in Fig. 6(iii); however, for this set of parameters, it is unstable. The eigenvalues and saddle-index associated with this point are shown in Table I.

Very close to the SNPs, the primary bifurcation curve undergoes PD bifurcations [see red \blacktriangledown in Fig. 6(a)], from where other *secondary* or *subsidiary* orbits emerge. The bifurcation curves

associated with two of those secondary orbits Γ_b^{s0} and Γ_b^{s1} are plotted in green in Fig. 6(a).

The change of the period-2 orbit Γ_b^{s1} around this diagram is shown in Figs. 7(i)–7(iii). This orbit is well illustrated in Fig. 7(i.2). As in the single-period case, the period diverges as we descend the green diagram [see Fig. 7(ii.1)] and approach ψ_e^β . The vicinity of this equilibrium leads to the characteristic spiral trajectory shown in Fig. 7(ii.2). Further decreasing $\|\psi\|$, Γ_b^{s1} approaches Hom_{s1}^b , where it is destroyed and the homoclinic orbit γ_b^{s1} is created. This state is known as a *two-homoclinic orbit* and is very similar to the orbit plotted in Fig. 7(iii).

Similarly, secondary orbits of a larger period arise from each of the PD bifurcations as one proceeds down in the diagram. Two of these curves are plotted in Figs. 6(b) and 6(c). Decreasing $\|\psi\|$, these orbits die at Hom_{s1}^b and Hom_{s2}^b , leading to new Shilnikov homoclinic orbits which occur very close to Hom_1^b . The characteristics of these orbits are also shown in Table I. This phenomenon is known as *homoclinic doubling cascade*,⁴⁶ and has been analyzed numerically.⁵² The main idea is that for $\Delta > \Delta_{\text{Hom}_1^b}$, an infinite number of N -homoclinic orbits γ_N (with $N > 0$) accumulate on the right side of the primary branch finishing at Hom_1^b .

The secondary green bifurcation curves $\Gamma_b^{s1,2,3}$ also undergoes PD bifurcation from where period-4 orbits emerge, leading to similar homoclinic doubling cascades. We represent this orbit as Γ_b^t , where the subindex t stands for *tertiary*. The bifurcation curve associated with Γ_b^t is shown in Fig. 6(d) together with Γ_b^{s1} . The modification of Γ_b^t along this diagram is shown in Figs. 7(iv)–7(vi). Proceeding down in the diagram, the modification of the orbits is similar to the single and period-2 cases. At Hom_{t1}^b a four-homoclinic orbit is formed. This orbit is similar to the long period limit cycle plotted in Fig. 7(vi).

The limit cycle Γ_a emerging from H_2^a [see left red curve in Fig. 5(a)] also undergoes an oscillatory damped structure around Hom_1^a . However, the oscillations in Δ are more damped. The period of Γ_a diverges as it approaches Hom_1^a , following the same oscillatory tendency [see Fig. 5(b)]. At Hom_1^a , the period of the oscillations becomes infinite, and Γ_a becomes the homoclinic orbit γ_a .

In contrast to the symmetrically driven case,³⁵ the absence of mirror symmetry prevents the existence of pairs of Shilnikov homoclinic orbits to a single symmetric saddle-focus equilibrium.

B. Saddle-loop homoclinic bifurcation

Increasing S , the previous scenario is modified as illustrated in Fig. 8(a) for $S = 5.5$. Here, $\text{Hom}_1^{a,b}$ are closer to one another. The features of these orbits are also shown in Table II. Furthermore, close to H_2^a , Γ_a undergoes a series of SNP and PDs, which were absent before. The divergence of the period close to Hom_1^a is depicted in Fig. 8(b).

In contrast to the situation shown for $S = 4.5$, the bifurcation curve Γ_c emerging from Hom_1^c (in purple) does not connect with H_2^b , but with a new homoclinic bifurcation Hom_2^a taking place at the saddle equilibrium ψ_e^ϵ . In this case [see a close-up view in Fig. 8(a)], the reconnection follows a monotonic growth in $\|\psi\|$ very different from the oscillatory one shown in the saddle-focus case. This saddle-loop homoclinic bifurcation, labeled Hom_2^a , is characterized by a scaling law $T \propto -\ln(\Delta - \Delta_{\text{Hom}_2^a})/a_u$, which governs the period

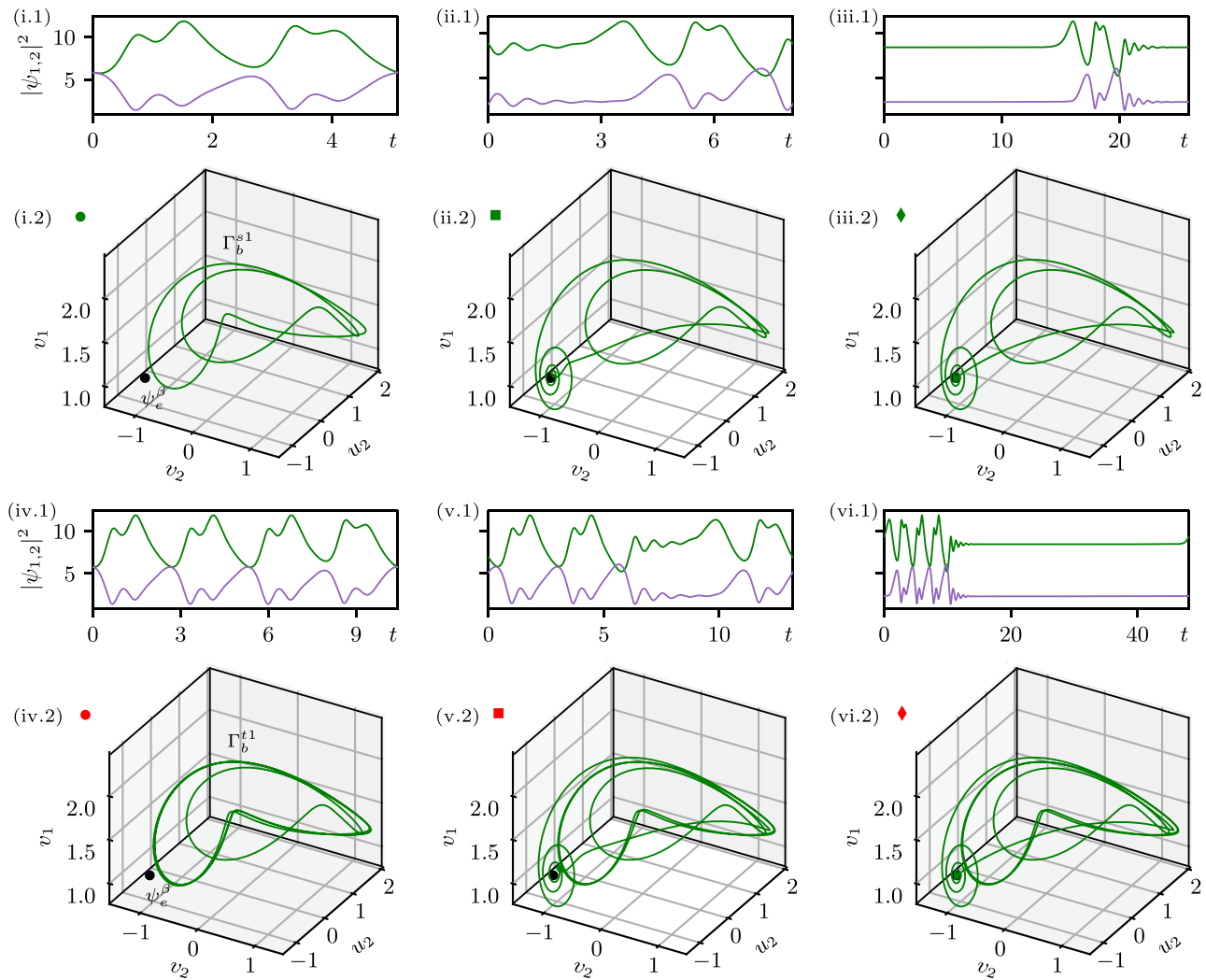


FIG. 7. Temporal trace and projection on the $\{(v_2, u_2, v_1)\}$ -subspace of the subsidiary and tertiary oscillatory states Γ_b^{s1} and Γ_b^{t1} . Panels (i)–(iii) show the modification of Γ_b^{s1} along its bifurcation curve in Fig. 6(a) (see green \bullet , \blacksquare , \blacklozenge). At $\text{Hom}_{s_1}^b$, a two-homoclinic orbit is created which is very similar to the state shown in (iii). Panels (iv)–(vi) show the modification of Γ_b^{t1} (see red \bullet , \blacksquare , \blacklozenge) along its bifurcation curve while approaching $\text{Hom}_{t_1}^b$ in Fig. 6(d). At $\text{Hom}_{t_1}^b$, a two-homoclinic orbit is created, which is very similar to the state shown in (vi).

of the oscillatory state very close to the bifurcation.⁷ This divergence is plotted in Fig. 8(c).

The limit cycle Γ_b emerging from H_2^b does not die at Hom_1^b , but at another saddle-loop homoclinic bifurcation Hom_2^b . These homoclinic orbits are unstable and, therefore, cannot be observed in direct numerical time simulations.

VI. CHAOTIC DYNAMICS

In this section, we analyze the emergence of chaotic dynamics, one close to $\Delta = C$, the other when $\Delta \gg C$, finding two main scenarios leading to chaos. The first one involves a period-doubling

cascade,⁸ while the second one is associated with the presence of a homoclinic bifurcation.³⁹

A. Period doubling cascade to chaos

As shown previously, the periodic orbits emerging from the different H bifurcations may encounter PD bifurcations, where period-2 orbits are created, while the former ones become unstable. This PD process might repeat in cascade and lead to temporal chaos. Figure 9(a) shows the occurrence of these bifurcations in a diagram, which depicts $|\psi_1|^2$ as a function of S for $C = \Delta = 5$. This diagram corresponds to a vertical slice of the phase diagram shown

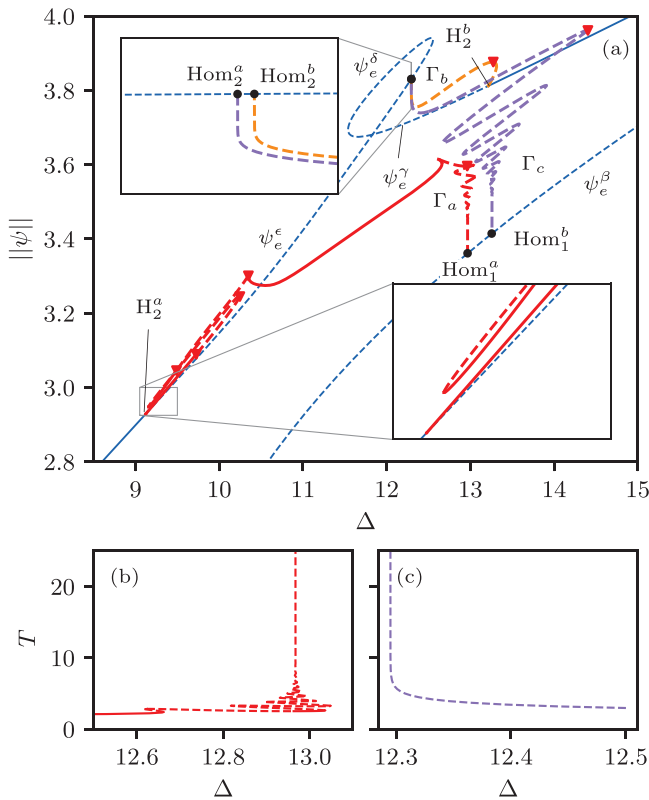


FIG. 8. (a) Bifurcation diagram showing $\|\psi\|$ as a function of Δ around the Shilnikov bifurcations $\text{Hom}_1^{a,b}$ and saddle-loop bifurcations $\text{Hom}_2^{a,b}$ for $C = 5$ and $S = 5.5$. (b) shows the divergence of the period of Γ_a around Hom_1^a , (c) shows the monotonic divergence of the period of Γ_c when approaching Hom_2^a .

in Fig. 4(a). We only plot the three equilibrium branches ψ_e^γ , ψ_e^δ , and ψ_e^ϵ , which are linked through the bifurcations SN_3^l and SN_3^r . The Hopf line H_1 cuts the stable branch at two points that we label $H_1^{a,b}$. From these points, the single-period limit cycle Γ_a appears supercritically. The periodic attractor associated with this orbit is plotted in the 3D phase subspace $\{(v_2, u_2, v_1)\}$ depicted in Fig. 9(i.1). The temporal trace is shown in Fig. 9(i.2).

TABLE II. Features and relevant information about the homoclinic bifurcations plotted in Fig. 8. SF stands for saddle-focus equilibrium, S corresponds to a saddle equilibrium, λ_s represents the stable eigenvalues, λ_u is an unstable real eigenvalue, and δ is the saddle-index associated with the homoclinic bifurcation.

Label	ψ_e -type	Δ	λ_u	λ_s	δ
Hom_2^a	S	12.2951	1.1762	-3.1762	2.700 30
Hom_2^b	S	12.2953	1.1134	-3.1134	2.796 20
Hom_1^a	SF	12.9672	3.4932	-1 - i9.7634	0.286 26
Hom_1^b	SF	13.2552	3.5641	-1 - i1.0048	0.280 57

On the left, this state undergoes a pair of SNPs where it loses and gains stability. Once SNP_2 is passed, Γ_a remains stable until PD_2 . This situation is shown in the close-up view plotted in Fig. 9(b). At PD_2 , an oscillatory state with two different periods, hereafter Γ_a^2 , emerges and remains stable until PD_4 . An example of this state is plotted in Fig. 9(ii). From PD_4 , a new oscillatory state, Γ_a^4 , emerges [see Fig. 9(iii)] and after that, a cascade of period-doubling bifurcations ($\text{PD}_8, \text{PD}_{16}$, etc.) occurs in a very short interval of S . From these bifurcations, the states Γ_a^8 [shown in Fig. 9(iv)] and Γ_a^{16} (not shown here) emerge. Increasing a bit further S , the system reaches a regime characterized by chaotic states like the one shown in Fig. 9(v).

After passing PD_2 , Γ_a^2 undergoes several SNPs and PDs for increasing values of S , and eventually, it connects back to Γ_a . The different limit cycles undergo several SNPs as shown in the close-up view in Fig. 9(a). A similar structure is found on the right part of the diagram close to H_1^b .

The period-doubling cascades are also illustrated through the *Feigenbaum diagram*⁸ plotted in Fig. 9(c). This diagram has been computed by scanning the stable attractors of the system as a function of S and collecting the local maxima and minima of the oscillatory states. The extension of this diagram corresponds to the shadowed gray box in Fig. 9(a). The close-up view corresponds to the range plotted in Fig. 9(b).

Increasing S , the chaotic attractor increases its morphological complexity and undergoes the typical windows of odd period oscillations.⁸ A complete understanding of these modifications, and the *crisis* suffered by the attractor, requires the analysis of its return map, as reported in Refs. 53 and 54. The chaotic nature of this system can be also characterized through the computation of the Lyapunov exponent and the Kaplan–Yorke dimension associated with the dynamics. This type of approach has been applied to investigate the route to chaos in a plasmonic dimer.⁵⁵ Such analyses are beyond the scope of this work.

The chaotic dynamics persist until a critical value of S , where the chaotic attractor collides with an unstable periodic orbit on its basin boundary and is destroyed. This is a typical phenomenon in chaotic dynamics and it is known as *boundary crisis*.⁸ We label this boundary crisis BC_1 as depicted in Figs. 9(a) and 9(c). After crossing this point, the only attractor of the system is the stable steady-state ψ_e^ϵ . Similarly, this route to chaos arises from H_1^b on the right and ends in a second BC_2 (not shown).

B. Chaos close to a Shilnikov homoclinic bifurcation

In this section, we analyze the emergence of chaotic dynamics close to homoclinic orbits. As stated by the Shilnikov theorem, if the Shilnikov bifurcation is wild (i.e., $\delta < 1$), chaotic dynamics is expected in the neighborhood of the homoclinic orbit.⁴⁶ The interplay between chaotic dynamics and homoclinic orbits has been studied by different authors, in particular, in the context of the Rossler model.^{48,56–58}

To illustrate this phenomenon, let us take a look at the curve shown in Fig. 10, which corresponds to the primary orbit Γ_b emerging from H_2^a and dying at Hom_1^b . This diagram is a detailed version of the one plotted in Figs. 5(a) and 6(a). The close-up views of the diagram around the first four SNPs are shown in the insets, together with the PD bifurcations PD_j^r , and the period-2 secondary branches

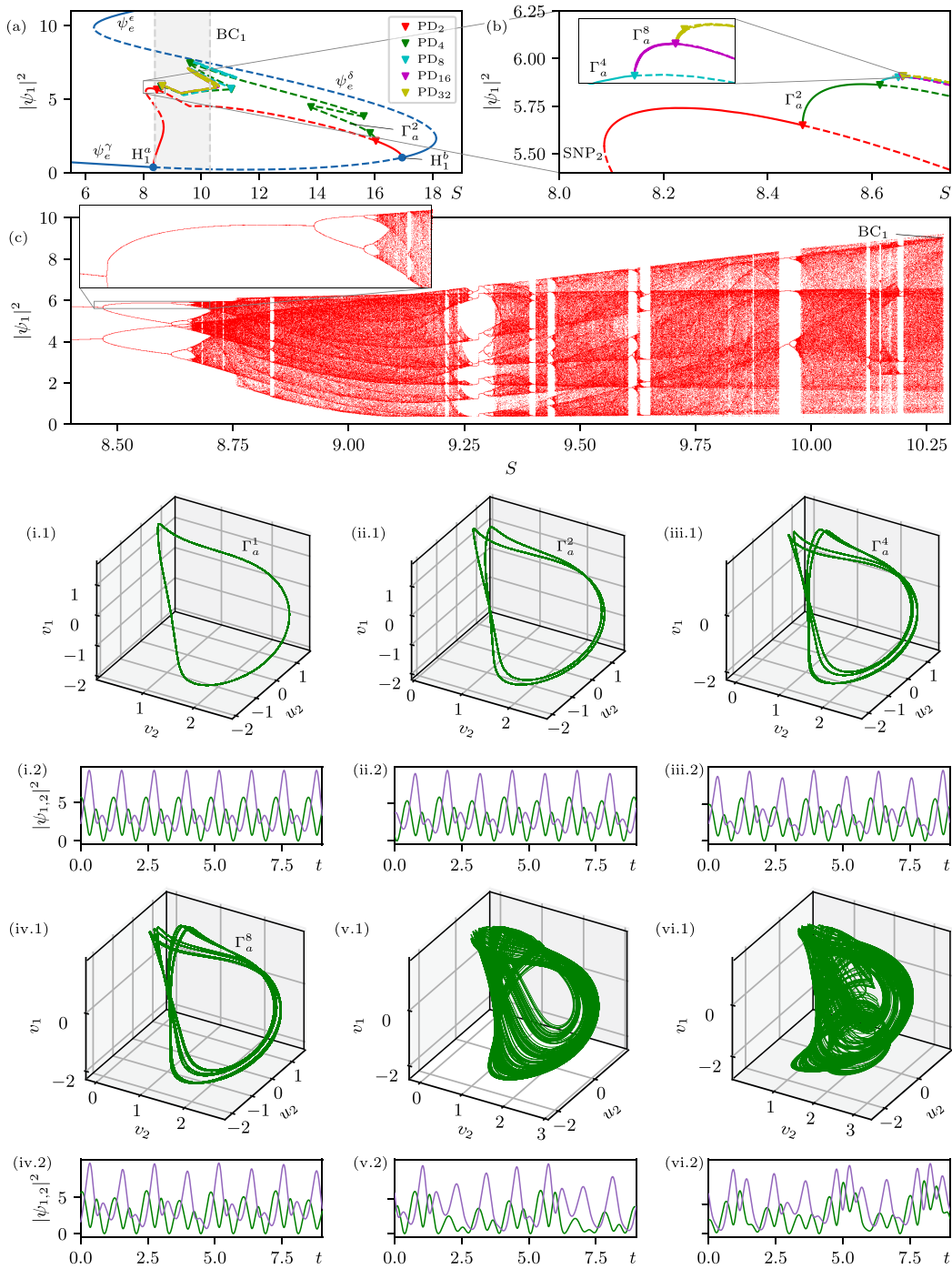


FIG. 9. Period doubling cascade and route to chaos for $C = \Delta = 5$. (a) shows the modification of the norm $|\psi_1|^2$ as a function of S . The different colored branches correspond to the oscillatory states with different periodicities. We mark the Hopf bifurcations H_1^a, H_1^b and different PD bifurcations. Solid (dashed) lines correspond to stable (unstable) states. Panel (b) is a close-up view of (a) around the period-doubling cascade. In (c), we plot the Feigenbaum diagram associated with the shadowed gray in (a), which shows the local maxima and minima modification of the dynamical attractors with changing S . Panels (i)–(vi) show the time trace (top panel) and projection of the attractors on the $\{v_2, u_2, v_1\}$ -subspace (bottom panels) for different values of S . From (i) to (vi), these values are, respectively, $S = 8.45, 8.50, 8.64, 8.84, 9.10, 10.26$. (v) and (vi) are chaotic attractors.

14 September 2023 07:25:06

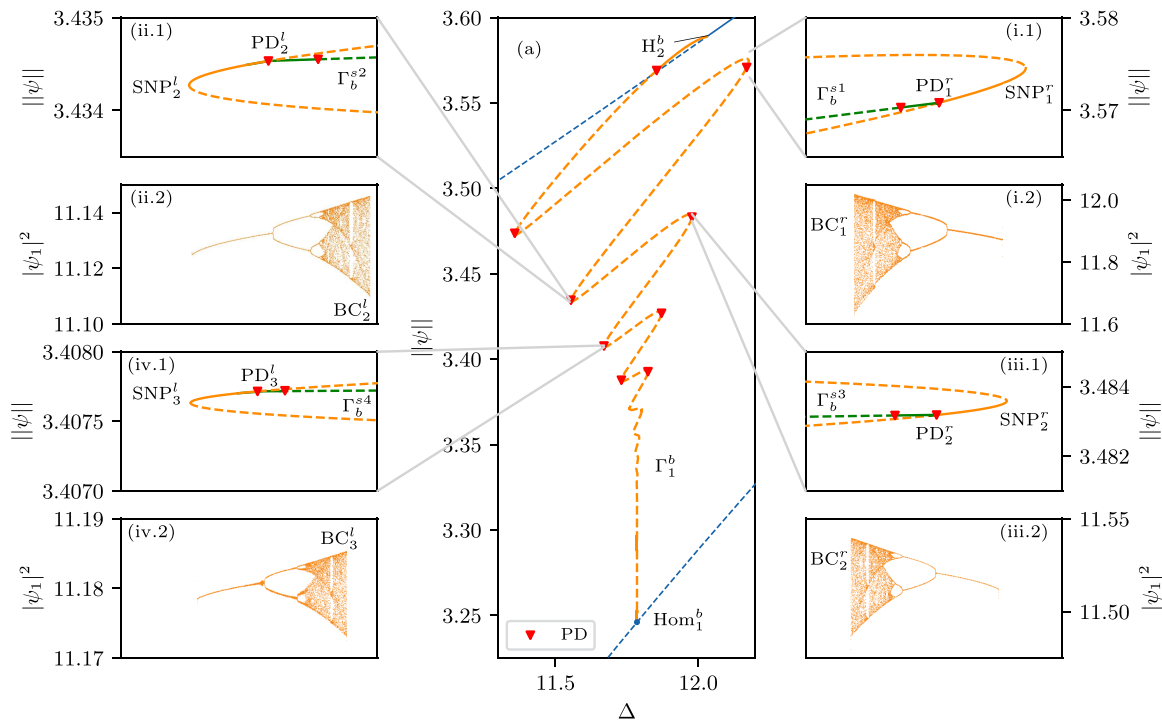


FIG. 10. Period doubling route to chaos near a wild Shilnikov homoclinic orbit. (a) shows the bifurcation curve of the principal periodic orbit Γ_b^b emerging from H_2^b and dying at Hom_1^b . Panels (i.1)–(iv.1) show a close-up view of (a) around SNP_1^r , SNP_2^l , SNP_2^r , and SNP_3^l , and the subsidiary dynamical state branches Γ_b^{s1-s4} . Panels (ii.2)–(iv.2) show the Feigenbaum diagram and standard period-doubling route to chaos corresponding to the same branches. The chaotic states die at several boundary crises $\text{BC}_j^{l,r}$.

emerging from them. These plots show a similar structure for the left and right folds and extend along with the whole diagram with decreasing $\|\psi\|$ (not shown here for simplicity). The panels below show the Feigenbaum diagrams for the same interval in S and the period-doubling cascade. The two types of diagrams on the onsets for the period-2 bifurcations show good agreement. With increasing S , each of these attractors undergoes a BC and they disappear.

All along this diagram, $\text{SNP}_i^{l,r}$ and $\text{BC}_i^{l,r}$ accumulate asymptotically around Hom_1^b and so do the chaotic regions. Eventually, the left and right BCs may collide, leading to the merging of the left and right chaotic attractors very close to Hom_1^b . Furthermore, while decreasing $\|\psi\|$ and approaching Hom_1^b , the chaotic attractor comes closer and closer to the SF ψ_e^b , and the trajectories must start to spiral around this point following the stable and unstable manifolds of ψ_e^b , in a similar manner as the one shown in Figs. 6 and 7 for the homoclinic orbits. The type of chaos associated with these attractors is commonly known as *spiral chaos*.^{57,58} However, due to the exponentially shrinking chaotic intervals when approaching Hom_1^b , we have not been able to confirm these two hypotheses.

VII. SUMMARY AND DISCUSSION

In this paper, we have presented a systematic study of the temporal dynamics arising in the asymmetrically driven dissipative photonic Bose–Hubbard dimer model. The particularity of this

system is that the coherent excitation is site-dependent. We here focused on the experimentally relevant case of a single excited site.^{21,25–32} This model has proved to describe very well the self-pulsing dynamics of two coupled photonic cavities under single beam excitation.^{25,26} Previous theoretical results have focused on the symmetrically driven model for which the excitation is site independent.^{34,35} These two configurations, however, lead to different bifurcation structures, which have important implications for the dimer dynamics. The main difference between them lies in the symmetry of the problem. While the symmetrically driven photonic dimer is invariant under the phase space mirror symmetry (i.e., under the swapping ψ_1 and ψ_2), this symmetry is intrinsically broken for single-site excitation. Due to this feature, in the symmetrically driven case, the standard solutions are symmetric, in the sense that $\psi_1 = \psi_2$, while asymmetric ones, satisfying $\psi_1 \neq \psi_2$, emerge through pitchfork symmetry breaking bifurcations.³⁵ Such pitchfork bifurcation is naturally absent in the asymmetrically driven PBHD studied here. Moreover, in this latter case, both the bonding-like (B) ($\psi_1 = \psi_2$) and the antibonding-like (AB) ($\psi_1 = -\psi_2$) modes can be linearly and nonlinearly excited. This is seen by the two resonances, located at $\Delta = \pm C$, appearing when scanning the detuning, the left (right) resonance corresponding to the excitation of the AB (B) mode of the photonic dimer. In the nonlinear regime, this leads to multistability and self-pulsing dynamics that have no counterparts in the symmetric case (see, for instance, Figs. 2–4).

Here, we have detailed the different static and dynamical regimes as a function of the driving field amplitude S . We have taken care to present our results by showing the modifications of the solution branches with respect to the detuning Δ . This allows for the physical interpretation of the dynamics in terms of resonances as well as a direct comparison with experimental results, which are usually obtained by scanning Δ for a fixed value of S . We focused on two different coupling rates: $C = 1.5$ corresponding to a weak coupling (WC) for which the resonance splitting is comparable to the resonance width of the uncoupled resonators, and $C = 5$ for which the resonators are strongly coupled (SC), and, hence, the two resonances are well separated. We observed that increasing the coupling makes the shape of the nonlinear resonances and the dynamics more and more complex. Moreover, for large drivings, while the fixed points have about the same amplitude in the two resonators ($|\psi_1| \approx |\psi_2|$) close to the left resonance, they are strongly different for the right one. This is reminiscent of the symmetry breaking appearing in nonlinear dimers with hidden \mathcal{PT} symmetry.⁵⁹

The linear stability of the homogeneous equilibrium points ψ_e against small perturbations shows the appearance of Hopf bifurcations where ψ_e states are destabilized in favor of periodically oscillating ones. In both coupling regimes, large relative oscillation amplitudes are detected (close to 100% contrast), which is of importance to make efficient parametric oscillators.²⁴ Moreover, the oscillations can emerge even in regions where bistability is absent. On the contrary, in symmetrically excited dimers, they occur in the bistability region generated by the pitchfork bifurcations.³⁵ In this latter case, the oscillation amplitudes are smaller, unless they trigger self-switching.

In contrast to the WC case, when the two resonances are initially well separated ($C = 5$), the bifurcation structure shows two distinct, yet connected, self-pulsing regions. The first one occurs within the SN_3 lines [see Fig. 4(a)] and is characterized by a resonant four-wave-mixing process for which the signal and idler photons are, respectively, on the B- and AB-like modes of the dimer. This corresponds to the self-pulsing dynamics reported in Refs. 25 and 49 for which the oscillation period is directly related to the resonance splitting. The second one appears beyond the cusp bifurcation C_1 and the corresponding parametric instability involves signal and idler photons on both the bonding- and antibonding-like modes, as for the self-pulsing encountered in the WC case.²⁶

We have also shown that the limit cycles emerging from the right resonance encounter a variety of homoclinic bifurcations where they die. By applying known results of dynamical systems theory,⁷ the study of these homoclinic bifurcations in the SC regime, allowed us to identify a homoclinic doubling cascade (see Fig. 6). Two main types of homoclinics have been identified: the first one is a closed orbit bi-asymptotic to a saddle-focus equilibrium (i.e., a Shilnikov homoclinic orbit), while the second one connects a saddle point with itself. In comparison, in the symmetrically driven model, solely Shilnikov homoclinic bifurcations appear, and they can only do it in pairs sharing a single saddle-focus equilibrium.^{34,35}

Chaos has been numerically found in the asymmetrically driven dissipative Bose–Hubbard dimers.¹⁵ We showed that chaotic dynamics emerge through several period-doubling cascades. One example of the bifurcation structure of such states is presented in Fig. 9. We have also analyzed the emergence of chaotic dynamics

close to the Shilnikov homoclinic bifurcations (see Fig. 10). Due to the absence of the pitchfork bifurcation, the chaotic dynamics found here differ from those arising in symmetrically driven systems. The latter are indeed characterized by episodes of dominance in power of one of the two cavities, interrupted by irregular switching events,^{34,35} which is not seen in asymmetrically driven dimers.

Depending on the type of application, different parameter regions may be of interest. Regarding self-pulsing dynamics, they are avoided for low coupling and high detuning values [see gray region in Fig. 3(a)], while they seem to be always present in the SC regime. Increasing the coupling between cavities, the system dynamics become much more complex. As a result, more complicated temporal dynamics, including chaos, may arise. Therefore, one should focus on strong coupling regimes for applications related to, for example, chaotic cryptography.⁶⁰ Furthermore, different types of excitable dynamics may arise in different parameter regions. Indeed, type I excitability has typically been found in the vicinity of homoclinic bifurcations, while excitability of type II could arise close to a canard explosion. These dynamics are essential for optical information processing and computation. For instance, they can be key for designing integrated networks of nonlinear optical cells⁶¹ and brain-inspired software and hardware.^{62,63} This study is, however, out of the scope of this work and will be reported elsewhere.⁴⁵

The complexity of the dynamics appearing in the driven dissipative PBHD model, and the fidelity of this model to describe coupled Kerr cavities suggest that those dynamical regimes may be reachable experimentally. Hence, we hope that these results will be relevant for experimental applications of driven dissipative Bose–Hubbard dimers as well to nonlinear topological photonic systems in the form of 1D chains or 2D arrays of coupled resonators.

ACKNOWLEDGMENTS

This work was supported by the Fonds de la Recherche Scientifique—FNRS under Grant No PDR.T.0104.19 and the European Research Council (ERC) under the European Union’s Horizon 2020 research and innovation program (Grant Agreement No. 757800). F.L. and P.P.-R. acknowledge the support of the Fonds de la Recherche Scientifique-FNRS). P.P.-R. acknowledges support from the European Union’s Horizon 2020 research and innovation programme under the Marie Skłodowska-Curie Grant Agreement No. 101023717.

AUTHOR DECLARATIONS

Conflict of Interest

The authors have no conflicts to disclose.

Author Contributions

J.Y.-S.: Performed all bifurcation and stability analysis of the model, and prepared all the figures of the paper. Participated in the discussions and corrections of the paper (equal). **S.-P. G.:** Supervised the research and discussed the results. Participated in the discussions and corrections of the paper (equal). **F.L.:** Supervised the research and discussed the results. Participated in the discussions and corrections of the paper (equal). **P.P.-R.:** Supervised the overall research

and wrote the paper. Participated in the discussions and corrections of the paper (equal).

DATA AVAILABILITY

The data that support the findings of this study are available from the corresponding author upon reasonable request.

REFERENCES

- ¹G. Nicolis, *Introduction to Nonlinear Science* (Cambridge University Press, Cambridge, 1995).
- ²A. Jenkins, "Self-oscillation," *Phys. Rep.* **525**, 167–222 (2013).
- ³A. M. Zhabotinsky, "A history of chemical oscillations and waves," *Chaos* **1**, 379–386 (1991).
- ⁴I. R. Epstein and J. A. Pojman, *An Introduction to Nonlinear Chemical Dynamics: Oscillations, Waves, Patterns, and Chaos* (Oxford University Press, 1998).
- ⁵J. R. Pomeroy, E. D. Sontag, and J. E. Ferrell, "Building a cell cycle oscillator: Hysteresis and bistability in the activation of Cdc2," *Nat. Cell Biol.* **5**, 346–351 (2003).
- ⁶J. Guckenheimer and P. J. Holmes, *Nonlinear Oscillations, Dynamical Systems, and Bifurcations of Vector Fields*, Applied Mathematical Sciences (Springer-Verlag, New York, 1983).
- ⁷P. Glendinning, *Stability, Instability and Chaos* (Cambridge University Press, Cambridge, 1994).
- ⁸E. Ott, *Chaos in Dynamical Systems*, 2nd ed. (Cambridge University Press, Cambridge, 2002).
- ⁹E. N. Lorenz, "Deterministic nonperiodic flow," *J. Atmos. Sci.* **20**, 130–141 (1963).
- ¹⁰V. Petrov, V. Gáspár, J. Masere, and K. Showalter, "Controlling chaos in the Belousov-Zhabotinsky reaction," *Nature* **361**, 240–243 (1993).
- ¹¹P. D. Drummond, K. J. McNeil, and D. F. Walls, "Non-equilibrium transitions in sub/second harmonic generation," *Opt. Acta* **27**, 321–335 (1980).
- ¹²L. A. Lugiato, L. M. Narducci, D. K. Bandy, and C. A. Pennise, "Breathing, spiking and chaos in a laser with injected signal," *Opt. Commun.* **46**, 64–68 (1983).
- ¹³T. L. Paoli and J. E. Ripper, "Coupled longitudinal mode pulsing in semiconductor lasers," *Phys. Rev. Lett.* **22**, 1085–1088 (1969).
- ¹⁴B. Maes, M. Fiers, and P. Bienstman, "Self-pulsing and chaos in short chains of coupled nonlinear microcavities," *Phys. Rev. A* **80**, 033805 (2009).
- ¹⁵J. Petráček, Y. Ekşioğlu, and A. Sterkhova, "Simulation of self-pulsing in Kerr-nonlinear coupled ring resonators," *Opt. Commun.* **318**, 147–151 (2014).
- ¹⁶V. Grigoriev and F. Biancalana, "Resonant self-pulsations in coupled nonlinear microcavities," *Phys. Rev. A* **83**, 043816 (2011).
- ¹⁷Y. Sato, Y. Tanaka, J. Upham, Y. Takahashi, T. Asano, and S. Noda, "Strong coupling between distant photonic nanocavities and its dynamic control," *Nat. Photonics* **6**, 56–61 (2012).
- ¹⁸F. Bessin, F. Copie, M. Conforti, A. Kudlinski, A. Mussot, and S. Trillo, "Real-time characterization of period-doubling dynamics in uniform and dispersion oscillating fiber ring cavities," *Phys. Rev. X* **9**, 41030 (2019).
- ¹⁹M. Virte, K. Panajotov, H. Thienpont, and M. Sciamanna, "Deterministic polarization chaos from a laser diode," *Nat. Photonics* **7**, 60–65 (2013).
- ²⁰C. Bruder, R. Fazio, and G. Schön, "The Bose-Hubbard model: From Josephson junction arrays to optical lattices," *Ann. Phys.* **14**, 566–577 (2005).
- ²¹A. Tikan, J. Riemensberger, K. Komagata, S. Hönl, M. Churav, C. Skehan, H. Guo, R. N. Wang, J. Liu, P. Seidler, and T. J. Kippenberg, "Emergent nonlinear phenomena in a driven dissipative photonic dimer," *Nat. Phys.* **17**, 604–610 (2021).
- ²²X. Xue, Y. Xuan, P.-H. Wang, Y. Liu, D. E. Leaird, M. Qi, and A. M. Weiner, "Normal-dispersion microcombs enabled by controllable mode interactions," *Laser Photonics Rev.* **9**, L23–L28 (2015).
- ²³S. Fujii, Y. Okabe, R. Suzuki, T. Kato, A. Hori, Y. Honda, and T. Tanabe, "Analysis of mode coupling assisted Kerr comb generation in normal dispersion system," *IEEE Photonics J.* **10**, 1–11 (2018).
- ²⁴Y. Dumeige and P. Féron, "Coupled optical microresonators for microwave all-optical generation and processing," *Opt. Lett.* **40**, 3237–3240 (2015).
- ²⁵N. Carlon Zambon, S. R. K. Rodriguez, A. Lemaître, A. Harouri, L. Le Gratiet, I. Sagnes, P. St-Jean, S. Ravets, A. Amo, and J. Bloch, "Parametric instability in coupled nonlinear microcavities," *Phys. Rev. A* **102**, 023526 (2020).
- ²⁶J. Yelo-Sarrión, P. Parra-Rivas, N. Englebert, C. M. Arabi, F. Leo, and S.-P. Gorza, "Self-pulsing in driven-dissipative photonic Bose-Hubbard dimers," *Phys. Rev. Res.* **3**, L042031 (2021).
- ²⁷C. Eichler, Y. Salathe, J. Mlynek, S. Schmidt, and A. Wallraff, "Quantum-limited amplification and entanglement in coupled nonlinear resonators," *Phys. Rev. Lett.* **113**, 110502 (2014).
- ²⁸S. R. K. Rodriguez, A. Amo, I. Sagnes, L. Le Gratiet, E. Galopin, A. Lemaître, and J. Bloch, "Interaction-induced hopping phase in driven-dissipative coupled photonic microcavities," *Nat. Commun.* **7**, 11887 (2016).
- ²⁹S. A. Miller, Y. Okawachi, S. Ramelow, K. Luke, A. Dutt, A. Farsi, A. L. Gaeta, and M. Lipson, "Tunable frequency combs based on dual microring resonators," *Opt. Express* **23**, 21527–21540 (2015).
- ³⁰X. Xue, X. Zheng, and B. Zhou, "Super-efficient temporal solitons in mutually coupled optical cavities," *Nat. Photonics* **13**, 616–622 (2019).
- ³¹S. Preu, H. G. L. Schwefel, S. Malzer, G. H. Döhler, L. J. Wang, M. Hanson, J. D. Zimmerman, and A. C. Gossard, "Coupled whispering gallery mode resonators in the terahertz frequency range," *Opt. Express* **16**, 7336–7343 (2008).
- ³²O. B. Helgason, F. R. Artega-Sierra, Z. Ye, K. Twayana, P. A. Andrekson, M. Karlsson, J. Schröder, and V. Torres-Company, "Dissipative solitons in photonic molecules," *Nat. Photonics* **15**, 305–310 (2021).
- ³³B. Garbin, A. Giraldo, K. Peters, N. Broderick, A. Spakman, F. Raineri, A. Levenson, S. Rodriguez, B. Krauskopf, and A. Yacomotti, "Spontaneous symmetry breaking in a coherently driven nanophotonic Bose-Hubbard dimer," *Phys. Rev. Lett.* **128**, 053901 (2022).
- ³⁴A. Giraldo, B. Krauskopf, N. G. R. Broderick, J. A. Levenson, and A. M. Yacomotti, "The driven-dissipative Bose-Hubbard dimer: Phase diagram and chaos," *New J. Phys.* **22**, 043009 (2020).
- ³⁵A. Giraldo, N. G. R. Broderick, and B. Krauskopf, "Chaotic switching in driven-dissipative Bose-Hubbard dimers: When a flip bifurcation meets a T-point in \mathbb{R}^4 ," *Discrete Contin. Dyn. Syst. B* **27**, 4023–4075 (2021).
- ³⁶E. J. Doedel, H. B. Keller, and J. P. Kernevez, "Numerical analysis and control of bifurcation problems (I): Bifurcation in finite dimensions," *Int. J. Bifurcation Chaos* **01**, 493–520 (1991).
- ³⁷E. J. Doedel, H. B. Keller, and J. P. Kernevez, "Numerical analysis and control of bifurcation problems (II): Bifurcation in finite dimensions," *Int. J. Bifurcation Chaos* **1**, 745–772 (1991).
- ³⁸E. J. Doedel, B. E. Oldeman, A. R. Champneys, F. Dercole, T. Fairgrieve, Y. A. Kuznetsov, R. Paffenroth, B. Sandstede, X. Wang, and C. Zhang, *AUTO-07p: Software for Continuation and Bifurcation Problems in Ordinary Differential Equations* (Concordia University, Montreal, 2007).
- ³⁹S. Wiggins, *Introduction to Applied Nonlinear Dynamical Systems and Chaos*, 2nd ed. (Springer, New York, 2003).
- ⁴⁰Y. Dumeige and P. Féron, "Dispersive tristability in microring resonators," *Phys. Rev. E* **72**, 066609 (2005).
- ⁴¹J. Prat, I. Mercader, and E. Knobloch, "The 1:2 mode interaction in Rayleigh-Bénard convection with and without Boussinesq symmetry," *Int. J. Bifurcation Chaos* **12**, 281–308 (2002).
- ⁴²K. Bold, C. Edwards, J. Guckenheimer, S. Guharay, K. Hoffman, J. Hubbard, R. Oliva, and W. Weckesser, "The forced van der Pol equation II: Canards in the reduced system," *SIAM J. Appl. Dyn. Syst.* **2**, 570–608 (2003).
- ⁴³E. M. Izhikevich, "Neural excitability, spiking and bursting," *Int. J. Bifurcation Chaos* **10**, 1171–1266 (2000).
- ⁴⁴P. Parra-Rivas, D. Gomila, M. A. Matias, P. Colet, and L. Gelens, "Competition between drift and spatial defects leads to oscillatory and excitable dynamics of dissipative solitons," *Phys. Rev. E* **93**, 012211 (2016).
- ⁴⁵J. Yelo-Sarrión, F. Leo, S.-P. Gorza, and P. Parra-Rivas, "Neuron-like spiking dynamics in the asymmetrically-driven dissipative photonic Bose-Hubbard dimer," *Phys. Rev. A* (published online, 2022).
- ⁴⁶A. J. Homburg and B. Sandstede, "Homoclinic and heteroclinic bifurcations in vector fields," in *Handbook of Dynamical Systems* (Elsevier Science, 2010), Vol. 3,

Chap. 8, pp. 379–524; available at <https://www.sciencedirect.com/science/article/pii/S1874575X10003164?via%3Dihub>.

- ⁴⁷A. Champneys, Y. A. Kuznetsov, and B. Sandstede, “A numerical toolbox for homoclinic bifurcation analysis,” *Int. J. Bifurcation Chaos* **06**, 867–887 (1996).
- ⁴⁸P. Glendinning and C. Sparrow, “Local and global behavior near homoclinic orbits,” *J. Stat. Phys.* **35**, 645–696 (1984).
- ⁴⁹D. Sarchi, I. Carusotto, M. Wouters, and V. Savona, “Coherent dynamics and parametric instabilities of microcavity polaritons in double-well systems,” *Phys. Rev. B* **77**, 125324 (2008).
- ⁵⁰M. Haelterman, S. Trillo, and S. Wabnitz, “Dissipative modulation instability in a nonlinear dispersive ring cavity,” *Opt. Commun.* **91**, 401–407 (1992).
- ⁵¹C. Laing and P. Glendinning, “Bifocal homoclinic bifurcations,” *Physica D* **102**, 1–14 (1997).
- ⁵²B. E. Oldeman, B. Krauskopf, and A. R. Champneys, “Death of period-doublings: Locating the homoclinic-doubling cascade,” *Physica D* **146**, 100–120 (2000).
- ⁵³O. E. Rössler, “Chaos in abstract kinetics: Two prototypes,” *Bull. Math. Biol.* **39**, 275–289 (1977).
- ⁵⁴R. Barrio, F. Blesa, and S. Serrano, “Qualitative analysis of the Rössler equations: Bifurcations of limit cycles and chaotic attractors,” *Physica D* **238**, 1087–1100 (2009).
- ⁵⁵Z. Ziani, G. Lévêque, S. Coulibaly, A. Taki, and A. Akjouj, “Investigating route to chaos in nonlinear plasmonic dimer,” *Ann. Phys.* **532**, 2000240 (2020).
- ⁵⁶A. Arneodo, P. Coulet, and C. Tresser, “Oscillators with chaotic behavior: An illustration of a theorem by Shil’nikov,” *J. Stat. Phys.* **27**, 171–182 (1982).
- ⁵⁷P. Gaspard and G. Nicolis, “What can we learn from homoclinic orbits in chaotic dynamics?,” *J. Stat. Phys.* **31**, 499–518 (1983).
- ⁵⁸S. Malykh, Y. Bakhanova, A. Kazakov, K. Pusuluri, and A. Shilnikov, “Homoclinic chaos in the Rössler model,” *Chaos* **30**, 113126 (2020).
- ⁵⁹Ş. K. Özdemir, S. Rotter, F. Nori, and L. Yang, “Parity-time symmetry and exceptional points in photonics,” *Nat. Mater.* **18**, 783–798 (2019).
- ⁶⁰M. S. Baptista, “Cryptography with chaos,” *Phys. Lett. A* **240**, 50–54 (1998).
- ⁶¹M. Brunstein, A. M. Yacomotti, I. Sagnes, F. Raineri, L. Bigot, and A. Levenson, “Excitability and self-pulsing in a photonic crystal nanocavity,” *Phys. Rev. A* **85**, 031803 (2012).
- ⁶²J. Feldmann, N. Youngblood, C. D. Wright, H. Bhaskaran, and W. H. Pernice, “All-optical spiking neurosynaptic networks with self-learning capabilities,” *Nature* **569**, 208–214 (2019).
- ⁶³J. Xiang, A. Torchy, X. Guo, and Y. Su, “All-optical spiking neuron based on passive microresonator,” *J. Lightwave Technol.* **38**, 4019–4029 (2020).